



Chromospheric heating and structure as determined from high resolution 3D simulations

M. Carlsson^{1,2}, V.H. Hansteen^{1,2}, and B.V. Gudiksen^{1,2}

¹ Institute of Theoretical Astrophysics, University of Oslo, P.O. Box 1029 Blindern, N-0315 Oslo, Norway

² Center of Mathematics for Applications, University of Oslo, P.O. Box 1052 Blindern, N-0316 Oslo, Norway

Abstract. We have performed 3D radiation MHD simulations extending from the convection zone to the corona covering a box 16 Mm^3 at 32 km spatial resolution. The simulations show very fine structure in the chromosphere with acoustic shocks interacting with the magnetic field. Magnetic flux concentrations have a temperature lower than the surroundings in the photosphere but higher in the low chromosphere. The heating is there mostly through ohmic dissipation preferentially at the edges of the flux concentrations. The magnetic field is often wound up around the flux concentrations. When acoustic waves travel up along the field this topology leads to swirling motions seen in chromospheric diagnostic lines such as the calcium infrared triplet.

Key words. Methods: numerical – hydrodynamics – MHD – radiative transfer – Stars: atmospheres

1. Introduction

Inferring physical conditions in the solar chromosphere is difficult, because the few spectral lines that carry information from this region (e.g. hydrogen Balmer- α , Ca II H and K lines and infrared triplet and He 1083 nm line) are formed outside local thermodynamic equilibrium (LTE). Thus they do not directly couple to the local conditions. In addition, the chromosphere is very dynamic with large variations in temperature and density and a concept like “formation height” is not very useful. We also go from plasma domination in the photosphere to a magnetically dominated regime in the upper chromosphere. This means that

the chromosphere can sustain a multitude of wavemodes that become degenerate and couple when the sound speed equals the Alfvén speed. Major progress in our understanding is dependent on comparison between detailed observations and detailed modelling. Such modelling needs to go all the way from the convection zone (where waves are excited and magnetic field foot-point braiding takes place) to the corona (to enable magnetic field connectivity) and include a reasonable treatment of the radiative transfer. The first such modelling was reported by Hansteen (2004). These simulations have been used to study flux emergence through the photosphere into the corona (Martínez-Sykora et al. 2008, 2009a) and driving of spicules (Martínez-Sykora et al. 2009b).

Send offprint requests to: M. Carlsson

We here analyze a high resolution simulation focusing on the chromospheric structure, heating and dynamics close to magnetic flux concentrations. The layout of this contribution is as follows: in Section 2 we outline the methods used, in Section 3 we describe how the simulation analyzed was set up, in Section 4 we give the results and we finish in Section 5 with conclusions.

2. Methods

Earlier simulations were carried out with the “Oslo Stagger Code”, a code where the parallelization was performed assuming shared memory and therefore restricted to rather few CPUs, see Hansteen, Carlsson, & Gudiksen (2007) for a description. We have now completed a full rewrite using the Message Passing Interface (MPI) parallelization library and a completely new radiation transfer module employing domain decomposition (Hayek et al. 2010). This new code, named BIFROST, is outlined below. A detailed writeup is in preparation (Gudiksen et al.).

We solve the equations of radiation-magnetohydrodynamics using a compact, high-order, finite difference scheme on a staggered mesh (6th order derivatives, 5th order interpolation). The equations are stepped forward in time using the explicit 3rd order predictor-corrector procedure of Hyman (1979), modified for variable time steps. High-order artificial diffusion is added both in the forms of a viscosity and in the form of a magnetic diffusivity. The radiative transfer equation is solved along 24 rays using a domain-decomposed short-characteristic method. The opacity from millions of spectral lines is included using multi-group opacities in four bins (Nordlund 1982) modified to include the effects of coherent scattering (Skartlien 2000). Conduction along the magnetic field-lines is solved implicitly using a multigrid method. In addition to the radiative energy exchange treated with the detailed solution of the radiative transfer (including scattering effects) we include optically thin radiative losses in the the corona and radiative losses from strong lines of hydrogen and singly

ionized calcium. These latter losses dominate the radiative losses from the chromosphere (Vernazza et al. 1981). We include these radiative losses without assuming LTE by using an expression

$$\Phi = \theta(T)e^{-\tau}f(\tau)$$

where Φ gives the radiative losses per electron per atom from a given element (hydrogen and singly ionized calcium, respectively), $\theta(T)$ is the sum of all collisional excitations (obtained from atomic data), T is temperature, τ is an optical depth and $e^{-\tau}f(\tau)$ is an effective escape probability. The optical depth τ is set proportional to the vertical column mass with the proportionality constant obtained from the 1D detailed non-LTE radiation hydrodynamic simulations of Carlsson & Stein (1992, 1995, 1997, 2002). The function $f(\tau)$ is obtained from a fit using the same 1D simulations.

3. Simulation setup

The simulation analyzed in this contribution covers a region $16.6 \times 16.6 \times 15.5 \text{ Mm}^3$ with the bottom boundary in the convection zone 1.4 Mm below the height where the mean optical depth at 500 nm is unity (in the following this height defines our $z=0$) and the top boundary in the corona 14.1 Mm above this height. Both the bottom and top boundaries are transparent. The simulation domain is periodic in both the horizontal directions with a fixed spacing of 32.5 km while the vertical grid size is 24-28 km up to 4 Mm height, increasing gradually above this height to a final maximum value of 213 km at the top of the computational domain. The final simulation has $512 \times 512 \times 325$ grid-points. The initial relaxation of the convection was performed at lower resolution.

The mean, unsigned field strength at $z=0$ is initially 40 G but falls to about 10 G at the beginning of the high-resolution run due to the fact that no field is injected into the computational domain and the existing, tangled field, decays slowly.

4. Results

After the increase of the resolution, there is a slow increase in the spatial power at high frequencies. After some 400 s the evolution starts to diverge from the continuation of the low resolution run — granules fragment more easily and the velocity power at small spatial scales increases. The mean unsigned field strength also starts to increase, presumably due to local dynamo action made possible at the higher resolution, and the mean unsigned field strength ends up at 15 G around $t=1500$ s and stays at this level until the end of the simulation at $t=1670$ s. The vertical magnetic field strength at $z=0$, $t=1500$ s is shown in Fig. 1. As can be expected from the low average unsigned field of 15 G there are large regions with only weak field. There are several regions with one polarity dominating but in general, both polarities co-exist. This is even more evident if the image scaling is adjusted to emphasize the weak field. The magnetic flux concentrations have a field strength close to 1 kG.

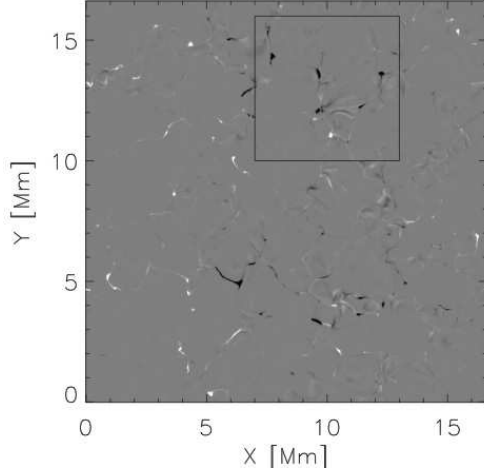


Fig. 1. Vertical magnetic field strength at $z=0$, $t=1500$ s. The colour scale has been clipped at 500 G to emphasize weaker field. The maximum field strength is ± 1 kG. The square marks the region of interest shown in more detail in Fig. 3.

The temperature structure of these magnetic flux concentrations compared with the

temperature structure of granules and intergranular lanes is shown in Fig. 2. The average temperature for granules has been taken over all columns with a vertical upflow larger than 100 m s^{-1} at $z=0$. The intergranular lane average has been taken over all columns with a vertical downflow larger than 100 m s^{-1} and the average for magnetic flux concentrations has been taken over all columns where the unsigned magnetic field in the photosphere is larger than 300 G. Intergranular lanes are hotter than granules above the surface (inverse granulation). Magnetic flux concentrations are cooler than intergranular lanes below the surface at a given geometric height but hotter than both granules and intergranular lanes in the upper photosphere and lower chromosphere.

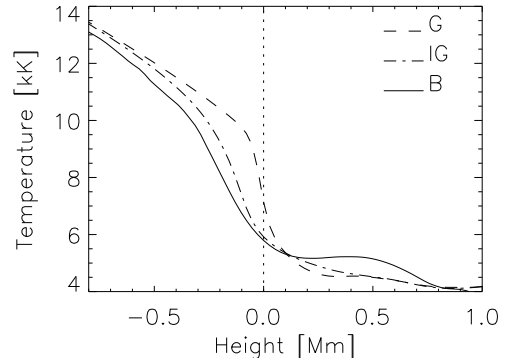


Fig. 2. Mean temperature as function of height for granules (dashed), intergranular lanes (dash-dotted) and magnetic flux concentrations (solid).

This increased temperature in the upper photosphere-lower chromosphere of magnetic flux concentrations is clearly shown in Fig. 3. The region shown with a square in Fig. 1 is shown in more detail at a height of 0.29 Mm with temperature, magnetic field strength, Joule heating and viscous heating displayed. It is clear that most magnetic flux concentrations have a higher temperature than the surroundings at this height and that Joule heating takes place at the locations of high magnetic field strength. These locations evolve only slowly in time while the viscous heating is concen-

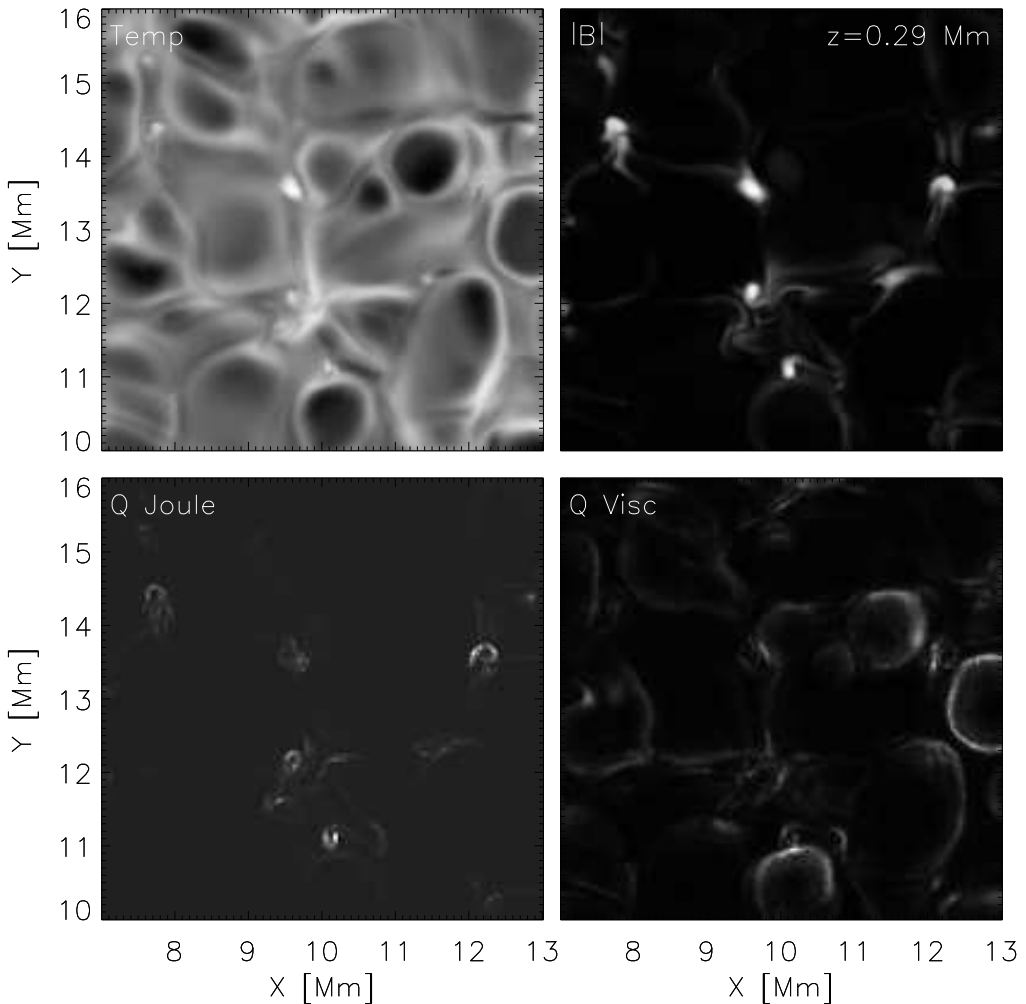


Fig. 3. Temperature (upper left panel), magnetic field strength (upper right), Joule heating (lower left) and viscous heating (lower right) at a height of 0.29 Mm at $t=1500$ s. At this height, magnetic flux concentrations are hotter than the surroundings due to Joule heating

trated at the edges of granules evolving on much shorter timescales.

Due to foot-point motions, the magnetic field topology in the chromosphere changes all the time. In the upper photosphere and lower chromosphere the plasma β (ratio between gas pressure and magnetic pressure) is larger than unity and the magnetic field is far from force-free. In the upper chromosphere, β drops below unity and the field approaches

a force-free state. This interplay between field-braiding and expansion into a force-free state often leads to spiral topologies around small magnetic flux concentrations. One example from the simulation is shown in Fig. 4 where the field-topology is shown around a magnetic flux concentration at $t=1010$ s. Field-lines from the negative polarity in the flux concentration connect to various positive polarity patches with a clear spiral pattern as

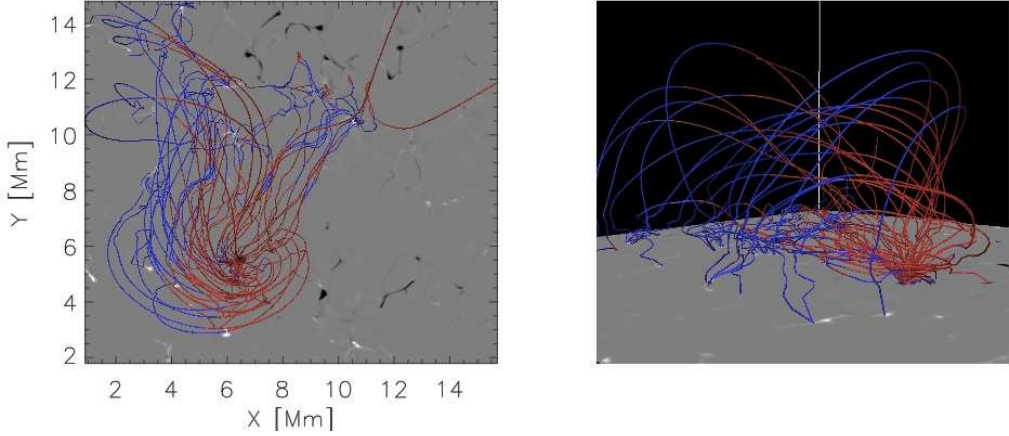


Fig. 4. Magnetic field above a magnetic field concentration as seen from above (*left panel*) and in perspective from the lower left corner (*right panel*). The vertical component of the field at $z=0$ is shown in greyscale. The sign of B_z is shown in colour with red field lines corresponding to negative B_z (dark in the plane at $z=0$). The highest field-lines shown extend to a height of 5.8 Mm. Note the spiral topology as seen from above and the abundance of low-lying almost horizontal field-lines.

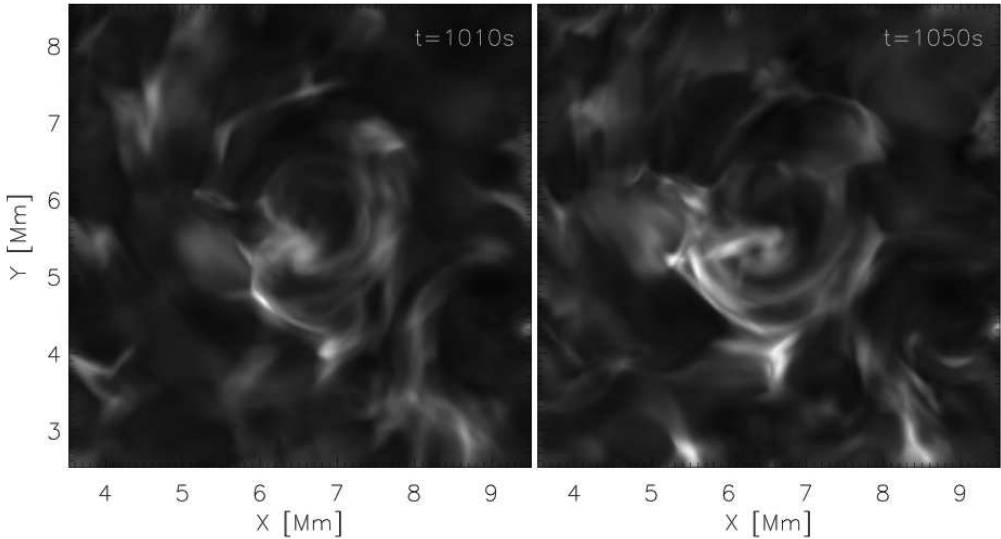


Fig. 5. Synthesized narrow band image at the core of the chromospheric $\lambda 854.2$ nm line from singly ionized calcium at two times showing the apparent swirling motion.

seen from above (left panel in Fig 4) and a large amount of almost horizontal (but curved) field (right panel in Fig 4). At this instant in time in the simulation there is an acoustic wave that turn into a slow-mode wave in the low- β region travelling along the curved field-lines.

In synthesized, narrow band, images from the core of the $\lambda 854.2$ nm line of singly ionized calcium (Fig.5) this is visible as a swirling motion around the flux-concentration very similar to observations recently reported by

Wedemeyer-Böhm & Rouppe van der Voort (2009).

5. Discussion and conclusions

A multitude of phenomena are seen in these high resolution radiation-MHD simulations that extend from the convection zone to the corona and we have here only focused on the heating and dynamics around magnetic flux concentrations. Although these simulations are the most ambitious performed to date, there are still important ingredients missing. The current simulations do not include the effects of out-of-equilibrium hydrogen ionization even though it is known that such effects are very important for the energy balance of especially the middle-higher chromosphere (Carlsson & Stein 2002; Leenaarts & Wedemeyer-Böhm 2006; Leenaarts et al. 2007). Including such effects would likely increase the amplitude of shocks in the middle chromosphere. Another limitation is the neglect of the back-radiation from the corona onto the upper chromosphere. This radiation would heat the chromosphere above about 1 Mm height (Carlsson & Stein 2002) but have little effect on the heights discussed in this contribution.

Acknowledgements. This research was supported by the Research Council of Norway through the grant “Solar Atmospheric Modelling” and through grants of computing time from the Programme for Supercomputing.

References

- Carlsson M., Stein R.F., 1992, *ApJ*, 397, L59
 Carlsson M., Stein R.F., 1995, *ApJ*, 440, L29
 Carlsson M., Stein R.F., 1997, *ApJ*, 481, 500
 Carlsson M., Stein R.F., 2002, *ApJ*, 572, 626
 Gudiksen B., Carlsson M., Hansteen V.H., et al., (in preparation)
 Hansteen V.H., 2004, In: A.V.Stepanov, E.E.Benevolenskaya, E.G.Kosovichev (eds.) IAU Symp. 223: Multi Wavelength Investigations of Solar Activity, 385–386
 Hansteen V.H., Carlsson M., Gudiksen B., 2007, In: P. Heinzel, I. Dorotovič, & R. J. Rutten (ed.) The Physics of Chromospheric Plasmas, vol. 368 of Astronomical Society of the Pacific Conference Series, 107–114
 Hayek W., Asplund M., Carlsson M., et al., 2010, *A&A*, (submitted)
 Hyman J.M., 1979, In: Advances in computer methods for partial differential equations - III; Proceedings of the Third International Symposium, Bethlehem, Pa., June 20-22, 1979. (A80-26663 09-64) New Brunswick, N.J., International Association for Mathematics and Computers in Simulation, 1979, p. 313-321., 313–321
 Leenaarts J., Wedemeyer-Böhm S., 2006, *A&A*, 460, 301
 Leenaarts J., Carlsson M., Hansteen V., Rutten R.J., 2007, *A&A*, 473, 625
 Martínez-Sykora J., Hansteen V., Carlsson M., 2008, *ApJ*, 679, 871
 Martínez-Sykora J., Hansteen V., Carlsson M., 2009a, *ApJ*, 702, 129
 Martínez-Sykora J., Hansteen V., DePontieu B., Carlsson M., 2009b, *ApJ*, 701, 1569
 Nordlund A., 1982, *A&A*, 107, 1
 Skartlien R., 2000, *ApJ*, 536, 465
 Vernazza J.E., Avrett E.H., Loeser R., 1981, *ApJS*, 45, 635
 Wedemeyer-Böhm S., Rouppe van der Voort L., 2009, *A&A*, 507, L9